

Synergy Between Experiment and Simulation in Describing the Electrochemical Performance of Mg-doped $\text{LiNi}_x\text{Co}_y\text{Mn}_z\text{O}_2$ Cathode Material of Lithium Ion Battery

Yu-Hao Huang^{1,2}, Hung-Lung Chou^{1,3}, Fu-Ming Wang^{1,3,*}, Bing-Joe Hwang^{3,4}, Shih-Chieh Liao², Tzu-Nung Huang², Chia-Hung Su⁵ and Hai-Hua Liu⁵

¹Graduate Institute of Applied Science and Technology, National Taiwan University of Science and Technology, Taipei, Taiwan

²Material and Chemical Laboratories, Industrial Technology Research Institute, Hsinchu, Taiwan

³Sustainable Energy Center, National Taiwan University of Science and Technology, Taipei, Taiwan

⁴Department of Chemical Engineering, National Taiwan University of Science and Technology, Taipei, Taiwan

⁵Department of Chemical Engineering, Ming-Chi University of Technology, Taipei, Taiwan

*E-mail: mccabe@mail.ntust.edu.tw

Received: 29 April 2013 / Accepted: 13 May 2013 / Published: 1 June 2013

Electrically powered vehicles (EV) are the next promising transportation candidate. However, energy storage in EVs is a critical issue if transportation needs are to be met. Recently, three element-layered structure materials of the type $\text{LiNi}_{0.5}\text{Co}_{0.2}\text{Mn}_{0.3}\text{O}_2$ have found application as cathodes in lithium ion batteries. However, the performance of this battery type over a wide temperature range is poor, and this limits its development into the EV market. We report the synthesis of Mg-doped $\text{Li}_{1.1}\text{Ni}_{0.497}\text{Mg}_{0.003}\text{Co}_{0.2}\text{Mn}_{0.3}\text{O}_2$, prepared by solid-state methods for the improvement of battery performance for EV applications. Differential scanning calorimetry (DSC) analysis revealed that doping with Mg significantly enhances the thermal structural stability of $\text{LiNi}_{0.5}\text{Co}_{0.2}\text{Mn}_{0.3}\text{O}_2$. Additionally, Mg doping increases discharge capacity by 5% and 10% for room- and low-temperature (10 °C) operation, respectively. The increase in thermal stability provided a 66% improvement in the cycle life at high-temperature (60 °C) operation.

Keywords: Lithium ion battery; layer structure; Mg doped; cathode; thermal stability; low/ high temperature

1. INTRODUCTION

Lithium ion batteries are the major energy source used by portable electronics and are a primary candidate for powering electric vehicles because of their high energy density and good

cyclability [1-5]. Lithium transition metal-oxide cathodes of the type $\text{Li}[\text{Ni}_x\text{Mn}_y\text{Co}_z]\text{O}_2$ are promising materials because of their high reversible capacity, low toxicity, and low cost of manufacture [6-13]. These complexes have a layered $\alpha\text{-NaFeO}_2$ -type structure, with Ni, Co, and Mn ion oxidation states of +2, +3, and +4, respectively, as determined by density functional theory (DFT) calculations and X-ray absorption spectroscopy (XAS) measurements [14]. These three ions serve different functions within the structure; Ni^{2+} is an electrochemically active ion, whereas the Mn^{4+} ion, with its octahedral coordination, provides structural stability, and the Co^{3+} ion suppresses cation mixing between 3a and 3b sites [15]. $\text{LiNi}_{1/3}\text{Mn}_{1/3}\text{Co}_{1/3}\text{O}_2$ is a commercially available material; it has a specific capacity of 185 mAh g^{-1} . However, cationic mixing of Ni and Li ions at 3b crystallographic sites within the $\text{LiNi}_{1/3}\text{Mn}_{1/3}\text{Co}_{1/3}\text{O}_2$ lattice deteriorates the long-term performance of the cells. Thus, Ni, Co, and Mn content must be manipulated to provide optimal performance of these materials. Katiyar et al. reported a $\text{LiNi}_{0.66}\text{Co}_{0.17}\text{Mn}_{0.17}\text{O}_2$ compound, prepared by substitution of Ni for Co and Mn. They designed the material using computational methods to elucidate an optimal composition that provided high energy density with good structural stability. $\text{LiNi}_{0.66}\text{Co}_{0.17}\text{Mn}_{0.17}\text{O}_2$ has a discharge capacity of 167 mAh g^{-1} at 1C, and exhibits only slow deterioration over the first 12 cycles [16]. Duh et al. reported doping with Mg to reduce cation mixing. They demonstrated that $\text{LiNi}_{0.57}\text{Mg}_{0.03}\text{Co}_{0.25}\text{Mn}_{0.15}\text{O}_2$ undergoes a low rate of cation mixing and offers good structural integrity with a clear phase-transition boundary, a discharge capacity of 199 mAh g^{-1} , and 79% retention after 20 cycles [17]. Although the performance is an improvement on previous formulations, battery fading still occurs too fast, and Duh did not identify a suitable Mg doping percentage to enhance the energy density of $\text{Li}[\text{Ni}_x\text{Mn}_y\text{Co}_z]\text{O}_2$.

We report our computational structural calculations, a model simulation, and an experimental study to determine the optimal amount of Mg dopant in $\text{LiNi}_{0.5}\text{Co}_{0.2}\text{Mn}_{0.3}\text{O}_2$ to maximize battery performance at low and high temperatures. We also discuss our differential scanning calorimetric (DSC) findings and the cycle performance at high temperature operation.

2. EXPERIMENTAL

2.1 Sample preparation

To prepare Mg-doped $\text{LiNi}_{0.5}\text{Co}_{0.2}\text{Mn}_{0.3}\text{O}_2$, the magnesium nitrate ($\text{Mg}(\text{NO}_3)_2 \cdot 6\text{H}_2\text{O}$) was dissolved into deionized water and stirred at room temperature ($25 \pm 2 \text{ }^\circ\text{C}$) for 30 min. 5 g of commercial $\text{Ni}_{0.5}\text{Co}_{0.2}\text{Mn}_{0.3}(\text{OH})_2$ (Henan Kelong New Energy Co., KL523) was then dispersed into the above magnesium nitrate solution (20 mL) with continual stirring. The mixing solution was heated at $100 \text{ }^\circ\text{C}$ until the water had evaporated, leaving black powder. Stoichiometric amounts of $\text{LiOH} \cdot \text{H}_2\text{O}$ (15% excess Li was used to compensate for possible Li loss during the sintering process [18]) were mixed with the black powder by a dual axle planet type common rotation mixer, with zirconia balls, for 2 h. The uniformly mixed powder was then heated at $900 \text{ }^\circ\text{C}$ for 8 h in an alumina crucible, to obtain the Mg-doped $\text{LiNi}_{0.5}\text{Co}_{0.2}\text{Mn}_{0.3}\text{O}_2$.

2.2 Characterization

The crystal structures of $\text{LiNi}_{0.5}\text{Co}_{0.2}\text{Mn}_{0.3}\text{O}_2$ and Mg-doped $\text{LiNi}_{0.5}\text{Co}_{0.2}\text{Mn}_{0.3}\text{O}_2$ materials were examined by X-ray diffraction spectroscopy (XRD) (Rigaku D/max-b spectrometer) using $\text{Cu K}\alpha$ radiation with $\lambda = 1.5406 \text{ \AA}$. The surface morphology of the powders was obtained using a scanning electron microscope (SEM) (JEOL JSM-6500F) equipped with an energy-dispersive spectrometer (EDS).

2.3 Cell fabrication

The 18650-type cells were assembled in a dry room (Dew point : -50 to approximately -60 °C), using a Celgard 2320 membrane as a separator and a double-sided cathode (thickness: 94 μm) and anode (thickness: 84 μm). The cathode consisted 89 wt% active material ($\text{LiNi}_{0.5}\text{Co}_{0.2}\text{Mn}_{0.3}\text{O}_2$ or Mg-doped $\text{LiNi}_{0.5}\text{Co}_{0.2}\text{Mn}_{0.3}\text{O}_2$), 4 wt% graphite powder KS-4 (Timcal), 2 wt% of Super P (Timcal), and 5 wt% polyvinylidene fluoride- PVDF (Kureha) as the binder. The composite electrode slurry was coated onto aluminum foil (Nippon foil) and dried for 5 min at 110–130 °C in air, followed by 6 h in a vacuum oven at 90 °C. The anode consisted of 96 wt% graphite (nature graphite) as the active material, 1 wt% of graphite powder KS-4 (Timcal), and 3 wt% of a water-based binder (LA-132). The electrode slurry was coated onto copper foil (Nippon foil) and dried for 5 min at 110–130 °C in air, followed by 6 h in a vacuum oven at 90 °C. The cathode and anode dimensions were 55 mm \times 950 mm and 57 mm \times 980 mm, respectively. The electrodes were baked at 90 °C under vacuum prior to assembly in a dry room. Approximately 6 mL of electrolyte was added followed by crimping the cell to seal it. The electrolyte comprised 1M LiPF_6 (Kishda) dissolved in a mixture of ethylene carbonate (EC) (Alfa-Aesar), propylene carbonate (PC) (Alfa-Aesar), dimethyl carbonate (DMC) (Alfa-Aesar), and ethylmethyl carbonate (EMC) (Alfa-Aesar) solvents in the volume ratio of 3:1:4:2 with 2 wt% of vinylene carbonate (VC) electrolyte additive.

2.4 Electrochemical measurements

A cathode half cell system was assembled in a coin cell, and its electrochemical properties were evaluated. Measurements were made using a potentiostat/galvanostat (HEKA-PG340 & CHI-608d), with a charge-discharge range of 2.0-4.0 V. The Randles-Sevcik equation (Eq. 1) was used to calculate the diffusion coefficient by plotting the peak current (i_p) and the square root of the scan rate ($v^{1/2}$) for both the micro-electrode and the composite electrode:

$$i_p = 2.69 \times 10^5 n^{3/2} A D^{1/2} C^* v^{1/2} \quad (1)$$

where i_p is the peak current in amperes, F is the Faraday constant, C^* is the initial concentration in mol cm^{-3} , v is the scan rate in Vs^{-1} , A is the electrode area in cm^2 , and D is the diffusion constant in cm^2s^{-1} .

Electrochemical impedance spectroscopy (EIS) was examined in the frequency range of 10M to 0.01 Hz with an AC amplitude of 5 mV.

The 18650 cells underwent galvanic cycling at room temperature (25 ± 2 °C) and at 60 °C at constant current; the electrochemical analyzer cut-off voltages were set to 2.8 V and 4.3 V. The coin cells were charged and discharged under constant current at ambient temperature (25 ± 2 °C) and at 10 °C, with the electrochemical analyzer cut-off voltages set during 2.8 V and 4.3 V versus the Li/Li⁺ reduction potential.

2.5 Thermal stability

The thermal stabilities of Mg-doped and non-doped $\text{LiNi}_{0.5}\text{Co}_{0.2}\text{Mn}_{0.3}\text{O}_2$ were studied using DSC (Perkin-Elmer, DSC 8500). The coin cell was charged to 4.3 V at 0.1 C and then disassembled in a glove box. The electrode was washed with DMC and the DMC medium was then removed in vacuum. Approximately 10 mg samples of the material were removed from the electrode by scraping and sealed in gold-plated high-pressure copper pans. DSC scans were conducted under nitrogen at a heating rate of 5 °C/min from 75 to 375 °C.

3. RESULTS AND DISCUSSION

3.1 Structural characterization

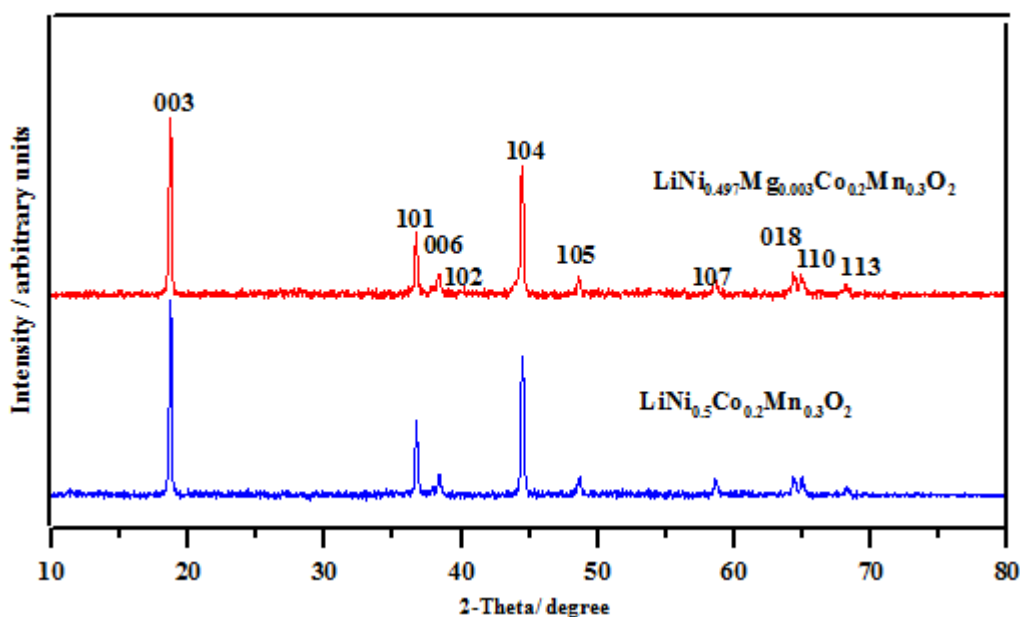


Figure 1. XRD spectrum of $\text{LiNi}_{0.5}\text{Co}_{0.2}\text{Mn}_{0.3}\text{O}_2$ and $\text{LiNi}_{0.497}\text{Mg}_{0.003}\text{Co}_{0.2}\text{Mn}_{0.3}\text{O}_2$.

Fig. 1 shows the XRD pattern and Miller indices for Mg-doped and non-doped $\text{LiNi}_{0.5}\text{Co}_{0.2}\text{Mn}_{0.3}\text{O}_2$. The main characteristic peaks were found at 2θ values of approximately 28° , 37° ,

38.6°, 44.5°, and 48°, corresponding to the (003), (101), (006), (104), (105), and, (107) planes, respectively. The figure shows that after sintering, the diffraction peaks of the two materials are obviously strong and intense, indicating perfect crystalline structures. The patterns also confirm that these two materials share the same single phase, the hexagonal α -NaFeO₂ structure with the $R\bar{3}m$ space group [19]. The XRD pattern for Mg-doped LiNi_{0.5}Co_{0.2}Mn_{0.3}O₂ shows an approximately 12% lower diffraction intensity compared to pristine LiNi_{0.5}Co_{0.2}Mn_{0.3}O₂, and does not contain peaks from any other crystal phases. Thus, Mg integrates into alternate layers of the [Ni_{0.5}Co_{0.2}Mn_{0.3}O₂](OH)₂ precursor, substituting at some Ni sites during the synthesis process. The presence of Mg does not alter the original Ni_{0.5}Co_{0.2}Mn_{0.3}O₂ structure. Compared to the directly synthesized precursor [Ni_xMg_yCo_zMn_mO₂](OH)₂, the proposed method provides a more stable compound. Because Mg²⁺ has a larger ionic radius ($r = 0.72 \text{ \AA}$) than Ni²⁺ ($r = 0.69 \text{ \AA}$), the lattice constants for Mg-doped LiNi_{0.5}Co_{0.2}Mn_{0.3}O₂ were $a = 2.8695 \text{ \AA}$ and $c = 14.2401 \text{ \AA}$, which are larger than the pristine LiNi_{0.5}Co_{0.2}Mn_{0.3}O₂ constants ($a = 2.8682 \text{ \AA}$ and $c = 14.2386 \text{ \AA}$). According to the reactant stoichiometry and the current XRD analysis, this study concludes that the Mg-doped LiNi_{0.5}Co_{0.2}Mn_{0.3}O₂ sample has the following stoichiometric formula: LiNi_{0.497}Mg_{0.003}Co_{0.2}Mn_{0.3}O₂. The (003) and (104) intensity ratios describe cation distribution within the lattice, and indicate the degree of cation mixing in LiNi_{0.5}Co_{0.2}Mn_{0.3}O₂ [17]. In the case of the current study, the (003) and (104) intensity ratios of LiNi_{0.497}Mg_{0.003}Co_{0.2}Mn_{0.3}O₂ for cation mixing is 1.33, indicating that this material has a layered structure with limited cation mixing. The appearance of intense (006)/(102) and (018)/(110) split peaks indicate a highly ordered layered structure, suggesting limited cation mixing in LiNi_{0.497}Mg_{0.003}Co_{0.2}Mn_{0.3}O₂.

3.2 DFT calculations and simulation

This study performed a theoretical simulation to establish a model for understanding the functional and energy characteristics of LiNi_{0.497}Mg_{0.003}Co_{0.2}Mn_{0.3}O₂. Based on the results from XRD patterns, the LiNi_{0.5}Co_{0.2}Mn_{0.3}O₂ and LiNi_{0.497}Mg_{0.003}Co_{0.2}Mn_{0.3}O₂ models can be represented as shown in Fig. 2. All assumptions and conditions of the parameter in the software is used to minimize the energy of the model and are listed in the figure. According to the proposed model, the system gradually relaxes to a balanced state at the energy minimum, indicating a stable structure. Convergence is achieved when electrical forces on the relaxed atoms are less than 0.01 eV/Å. From the study calculations, the total energy of each system exhibits a similar convergent trend after several dozen iterations (Fig. 3). For DFT calculations, the Vienna ab initio simulation package (VASP) [26-29] implements projector-augmented waves (PAW) [20-23] and generalized gradient approximation (GGA) [24-25]. For plane wave calculations, the total energy convergence calculation for the LiNi_{0.5}Co_{0.2}Mn_{0.3}O₂ (100) slab and the LiNi_{0.497}Mg_{0.003}Co_{0.2}Mn_{0.3}O₂ (100) slab systems gave a cut-off energy of 400 eV. To model the LiNi_{0.5}Co_{0.2}Mn_{0.3}O₂ (100) surface, slabs containing seven layers were adopted, with 12 atoms per layer, as shown in Fig. 2a and 2c. The surface is constructed as a slab within 3D periodic boundary conditions, and models are separated from their images in a direction perpendicular to the surface by a 14 Å vacuum layer.

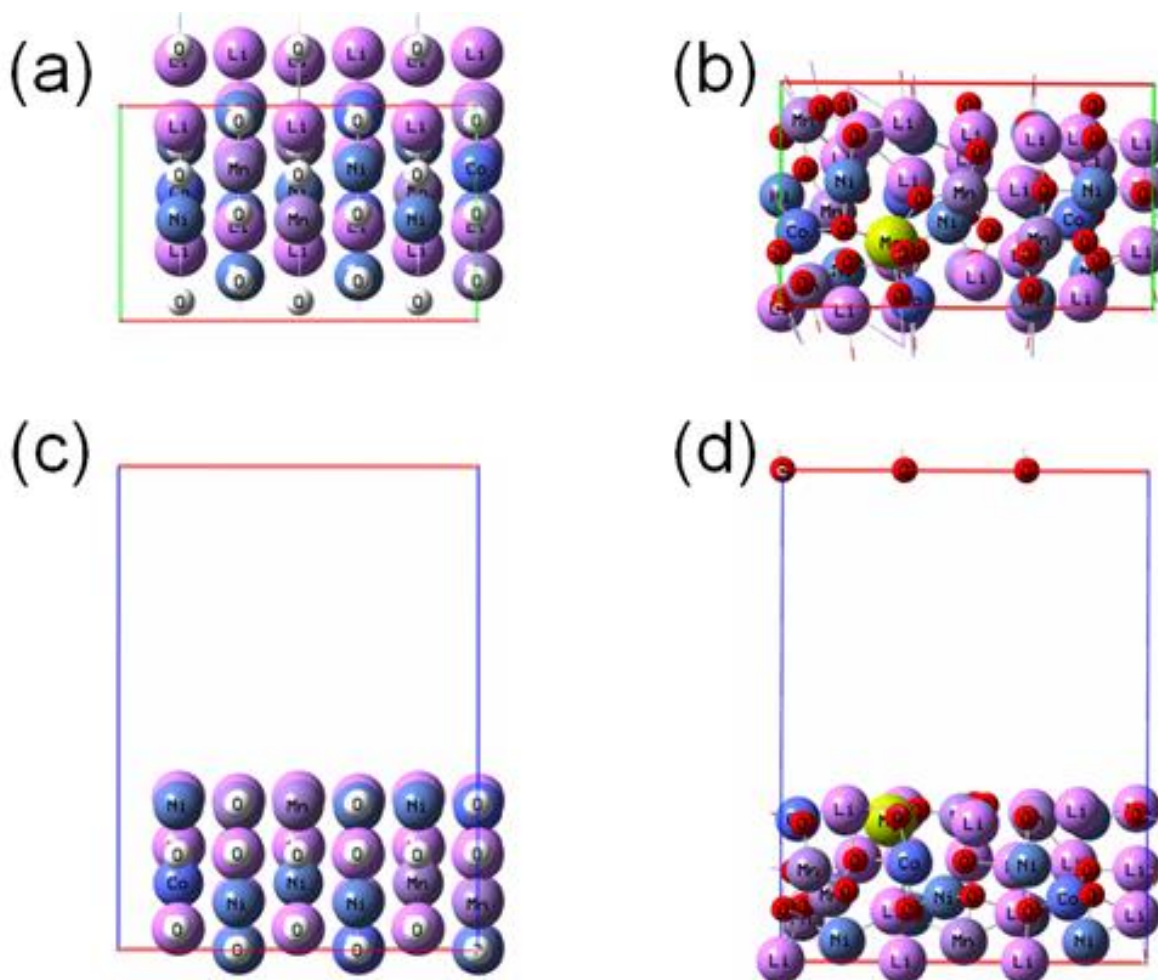


Figure 2. The model of (a) top-view of $\text{LiNi}_{0.5}\text{Co}_{0.2}\text{Mn}_{0.3}\text{O}_2(100)$, and (b) top-view of $\text{LiNi}_{0.497}\text{Mg}_{0.003}\text{Co}_{0.2}\text{Mn}_{0.3}\text{O}_2(100)$, and (c) side-view of $\text{LiNi}_{0.5}\text{Co}_{0.2}\text{Mn}_{0.3}\text{O}_2(100)$, and (d) side-view of $\text{LiNi}_{0.497}\text{Mg}_{0.003}\text{Co}_{0.2}\text{Mn}_{0.3}\text{O}_2(100)$, respectively.

The bottom two layers are kept fixed to the bulk coordinates; full atomic relaxations were allowed for the top five layers. For these calculations, a $3 \times 3 \times 1$ k -Point mesh was used for the 3×3 super cell. In the $\text{LiNi}_{0.5}\text{Co}_{0.2}\text{Mn}_{0.3}\text{O}_2(100)$ model, the super cell dimensions were $14.06 \times 8.45 \times 18.87 \text{ \AA}^3$.

The atoms in the model were allowed to relax until the forces on unconstrained atoms were less than 0.01 eV/\AA .

The results show that $\text{LiNi}_{0.497}\text{Mg}_{0.003}\text{Co}_{0.2}\text{Mn}_{0.3}\text{O}_2$ has less total energy (-480.54 eV) than $\text{LiNi}_{0.5}\text{Co}_{0.2}\text{Mn}_{0.3}\text{O}_2$ (-369.96 eV), indicating that Mg doping provides a relaxation interaction within the lattice that maintains the $\text{LiNi}_{0.5}\text{Co}_{0.2}\text{Mn}_{0.3}\text{O}_2$ structure in a balanced state at an energy minima. The data also demonstrate that $\text{LiNi}_{0.497}\text{Mg}_{0.003}\text{Co}_{0.2}\text{Mn}_{0.3}\text{O}_2$ is stable at high temperatures because of its highly stable infrastructure.

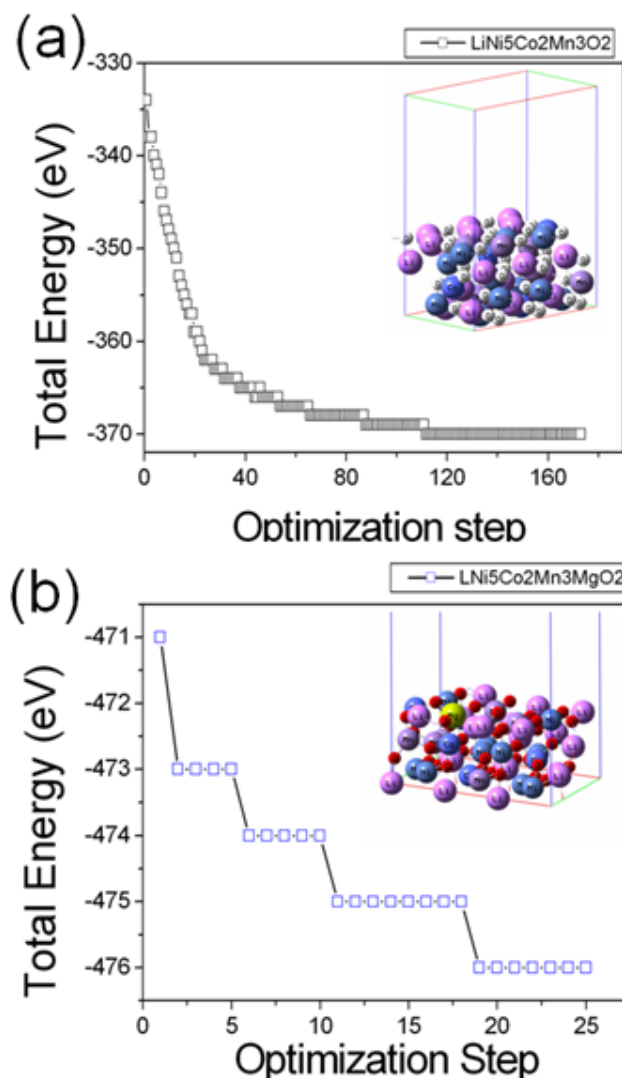


Figure 3. Calculated energy for (a) $\text{LiNi}_{0.5}\text{Co}_{0.2}\text{Mn}_{0.3}\text{O}_2(100)$, inset figure shows alternative-view of $\text{LiNi}_{0.5}\text{Co}_{0.2}\text{Mn}_{0.3}\text{O}_2$, and (b) $\text{LiNi}_{0.497}\text{Mg}_{0.003}\text{Co}_{0.2}\text{Mn}_{0.3}\text{O}_2$ (100) slab, respectively. Inset figure shows alternative-view of $\text{LiNi}_{0.5}\text{Co}_{0.2}\text{Mn}_{0.3}\text{MgO}_2$.

3.3 SEM morphology, diffusivity, and thermal stability

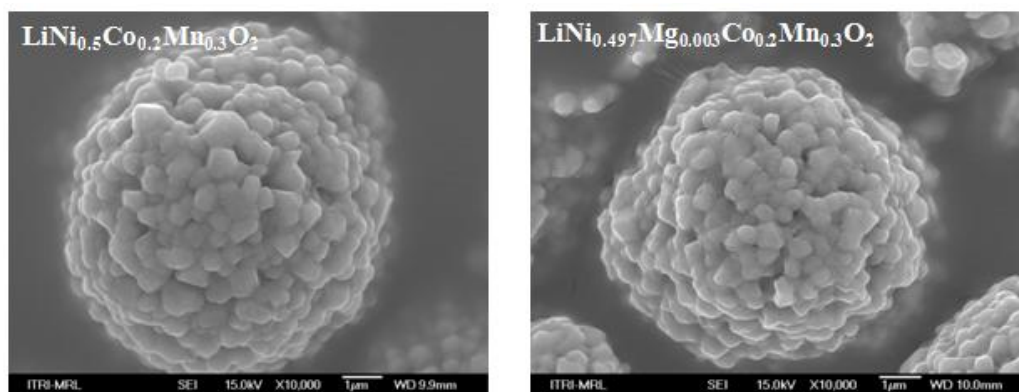


Figure 4. The SEM images of $\text{LiNi}_{0.5}\text{Co}_{0.2}\text{Mn}_{0.3}\text{O}_2$ and $\text{LiNi}_{0.497}\text{Mg}_{0.003}\text{Co}_{0.2}\text{Mn}_{0.3}\text{O}_2$.

Fig. 4 shows SEM images of $\text{LiNi}_{0.5}\text{Co}_{0.2}\text{Mn}_{0.3}\text{O}_2$ and $\text{LiNi}_{0.497}\text{Mg}_{0.003}\text{Co}_{0.2}\text{Mn}_{0.3}\text{O}_2$. These two materials are spherical secondary particles and their morphologies are similar. The secondary particle sizes (D50) of $\text{LiNi}_{0.5}\text{Co}_{0.2}\text{Mn}_{0.3}\text{O}_2$ and $\text{LiNi}_{0.497}\text{Mg}_{0.003}\text{Co}_{0.2}\text{Mn}_{0.3}\text{O}_2$ are in the range of 8-9 nm, suggesting that Mg doping does not affect the morphology of the original $\text{LiNi}_{0.5}\text{Co}_{0.2}\text{Mn}_{0.3}\text{O}_2$.

We used the Randles-Sevcik equation to describe the Li^+ ion diffusion behavior in the context of either $\text{LiNi}_{0.5}\text{Co}_{0.2}\text{Mn}_{0.3}\text{O}_2$ or $\text{LiNi}_{0.497}\text{Mg}_{0.003}\text{Co}_{0.2}\text{Mn}_{0.3}\text{O}_2$. The diffusion coefficient is estimated from a plot of the scan rate versus the anodic peak current (I_{pa}). The red dashed line shown in the figure for $\text{LiNi}_{0.497}\text{Mg}_{0.003}\text{Co}_{0.2}\text{Mn}_{0.3}\text{O}_2$ has a slope of $1.091 \times 10^{-12} \text{ cm}^2\text{s}^{-1}$. The black solid line, representing $\text{LiNi}_{0.5}\text{Co}_{0.2}\text{Mn}_{0.3}\text{O}_2$ (Fig. 5), has a lower slope of $8.751 \times 10^{-13} \text{ cm}^2\text{s}^{-1}$. Thus, the $\text{LiNi}_{0.497}\text{Mg}_{0.003}\text{Co}_{0.2}\text{Mn}_{0.3}\text{O}_2$ unit cell volume is increased by Mg doping because of the larger ionic radius of Mg^{2+} compared to Ni^{2+} . Accordingly, lithium ions can easily diffuse through the augmented lattice spaces, thus enhancing ionic transfer rates. Fig. 6 shows DSC profiles for $\text{LiNi}_{0.5}\text{Co}_{0.2}\text{Mn}_{0.3}\text{O}_2$ and $\text{LiNi}_{0.497}\text{Mg}_{0.003}\text{Co}_{0.2}\text{Mn}_{0.3}\text{O}_2$ after charging to 4.3 V. The integrated area in the exothermic direction represents the amount of heat generated from material decomposition, which results from the release of oxygen [30]. The figure clearly shows that the $\text{LiNi}_{0.497}\text{Mg}_{0.003}\text{Co}_{0.2}\text{Mn}_{0.3}\text{O}_2$ exothermic onset temperature is shifted from 291 to 298 °C. In addition, the exothermic heat associated with material decomposition at higher temperatures is also reduced from 516 to 500 J/g.

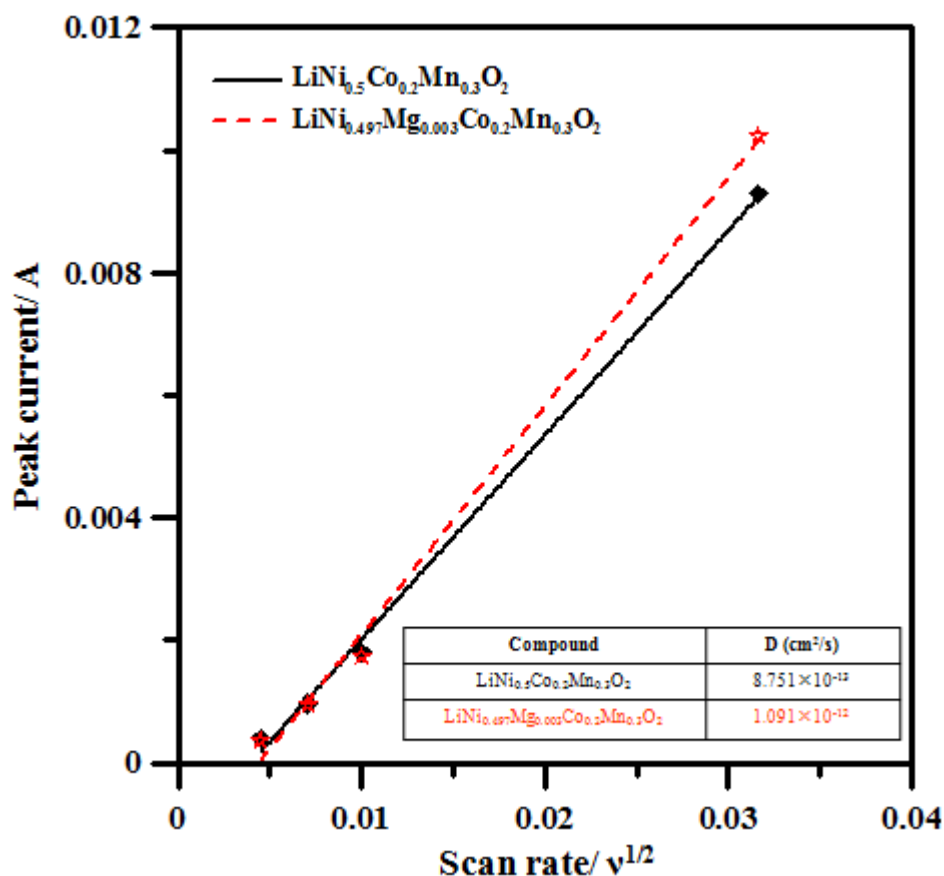


Figure 5. Cyclic voltammetry of $\text{LiCo}_{0.5}\text{Ni}_{0.2}\text{Mn}_{0.3}\text{O}_2$ and $\text{LiNi}_{0.497}\text{Mg}_{0.003}\text{Co}_{0.2}\text{Mn}_{0.3}\text{O}_2$ to derive lithium ion diffusion coefficient. The relationship of the peak current (i_p) and the square root of scan rate ($v^{1/2}$)

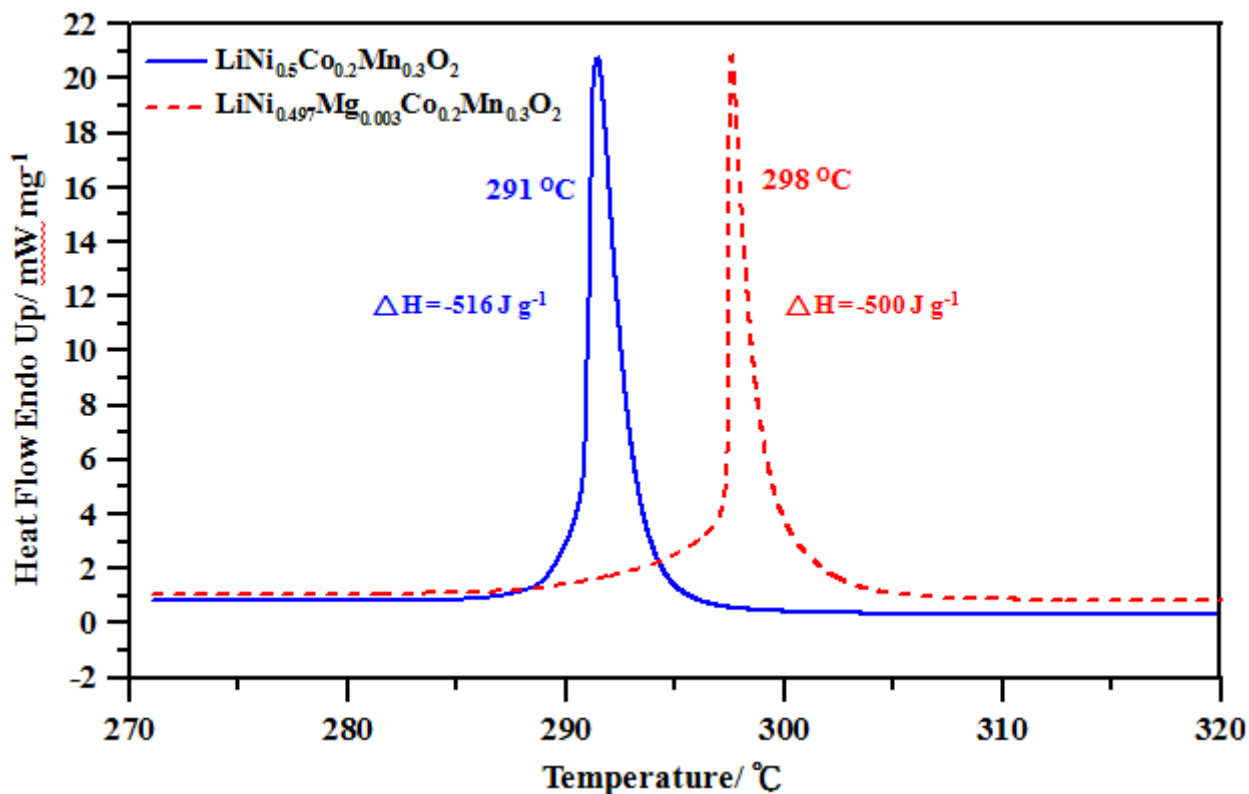


Figure 6. Differential scanning calorimetry profiles of $\text{LiNi}_{0.5}\text{Co}_{0.2}\text{Mn}_{0.3}\text{O}_2$ and $\text{LiNi}_{0.497}\text{Mg}_{0.003}\text{Co}_{0.2}\text{Mn}_{0.3}\text{O}_2$ after charged to 4.3V vs. Li/Li^+ .

These results indicate that Mg doping improves the thermal stability of $\text{LiNi}_{0.497}\text{Mg}_{0.003}\text{Co}_{0.2}\text{Mn}_{0.3}\text{O}_2$ because the presence of Mg^{2+} cations in the inter-slab space provides structural stability and maintains existing Mn-O bonds [30].

3.4 Electrochemical performance

In order to evaluate the amount effects of Mg doping into $\text{LiNi}_{0.5}\text{Co}_{0.2}\text{Mn}_{0.3}\text{O}_2$ structure, the 0.3 mol % and 3 mol % of Mg has been used to replace Ni position. Fig. 7a presents the charge and discharge curves of $\text{LiNi}_{0.5}\text{Co}_{0.2}\text{Mn}_{0.3}\text{O}_2$, $\text{LiNi}_{0.497}\text{Mg}_{0.003}\text{Co}_{0.2}\text{Mn}_{0.3}\text{O}_2$ and $\text{LiNi}_{0.47}\text{Mg}_{0.03}\text{Co}_{0.2}\text{Mn}_{0.3}\text{O}_2$. It is clear to observe that the discharge capacity has been improve by Mg doping. The discharge capacity of $\text{LiNi}_{0.497}\text{Mg}_{0.003}\text{Co}_{0.2}\text{Mn}_{0.3}\text{O}_2$ and $\text{LiNi}_{0.47}\text{Mg}_{0.03}\text{Co}_{0.2}\text{Mn}_{0.3}\text{O}_2$ show 167 and 164 mAh g⁻¹, which are all greater than $\text{LiNi}_{0.5}\text{Co}_{0.2}\text{Mn}_{0.3}\text{O}_2$. However, the discharge curves cannot reveal the difference to the amount effects of Mg doping. Fig. 7b shows the incremental capacity analysis of discharge curves of three samples. According to this figure, the curves of $\text{LiNi}_{0.497}\text{Mg}_{0.003}\text{Co}_{0.2}\text{Mn}_{0.3}\text{O}_2$ and $\text{LiNi}_{0.47}\text{Mg}_{0.03}\text{Co}_{0.2}\text{Mn}_{0.3}\text{O}_2$ slightly shift to the left side, representing the 0.3 mol % of Mg doping influences the average working voltage of cathodic reaction. This polarization is more obvious when the 3 mol % of Mg has doped into $\text{LiNi}_{0.5}\text{Co}_{0.2}\text{Mn}_{0.3}\text{O}_2$, indicating a serious electrochemical reaction of Mg takes place. In addition, the 3 mol % of Mg ion reduction and its reduction reaction potential also reveal clearly at 3.68V (a shoulder transition potential) rather than 0.3 mol % of Mg ion. Therefore, the

above analysis shows 3 mol % of Mg is too much that doped into $\text{LiNi}_{0.5}\text{Co}_{0.2}\text{Mn}_{0.3}\text{O}_2$, although the discharge capacity has been improved. A microelectrode linked cyclic voltammetry [31] will be employed to evaluate the intrinsic diffusion properties and the Mg doping effects of the bulk $\text{LiNi}_{0.497}\text{Mg}_{0.003}\text{Co}_{0.2}\text{Mn}_{0.3}\text{O}_2$ in which compares $\text{LiNi}_{0.5}\text{Co}_{0.2}\text{Mn}_{0.3}\text{O}_2$.

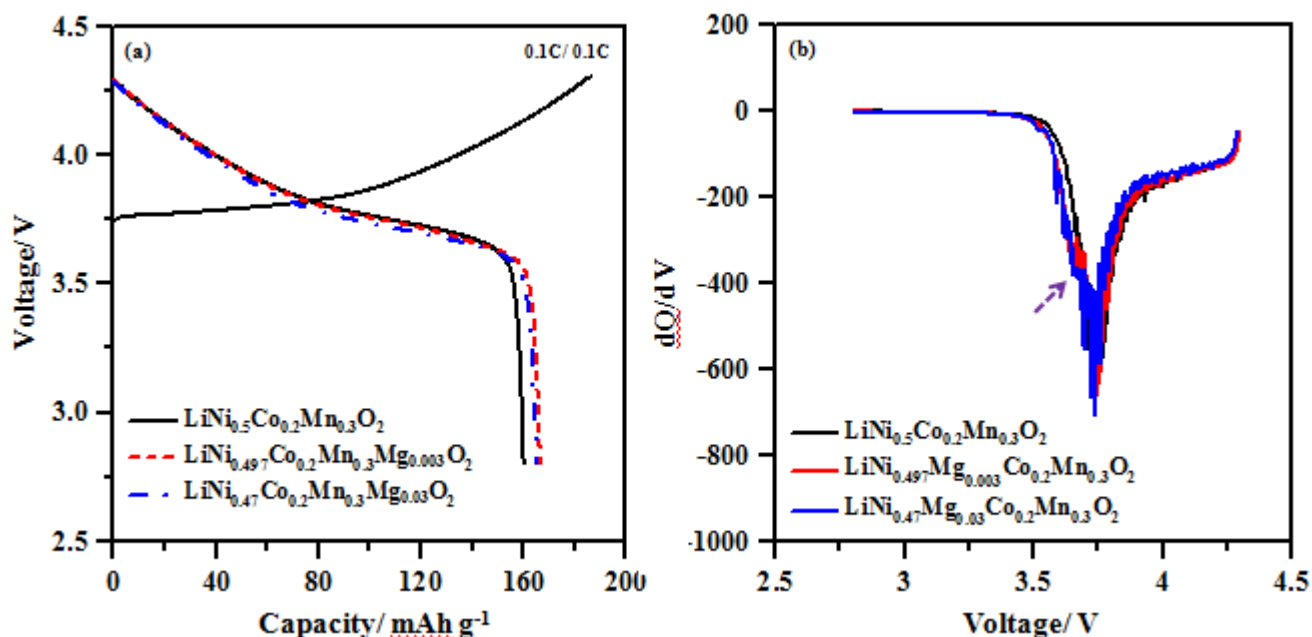


Figure 7. (a) The charge-discharge curves and (b) the incremental capacity of discharge curve of $\text{LiNi}_{0.5}\text{Co}_{0.2}\text{Mn}_{0.3}\text{O}_2$, $\text{LiNi}_{0.497}\text{Mg}_{0.003}\text{Co}_{0.2}\text{Mn}_{0.3}\text{O}_2$ and $\text{LiNi}_{0.47}\text{Mg}_{0.03}\text{Co}_{0.2}\text{Mn}_{0.3}\text{O}_2$ at room temperature.

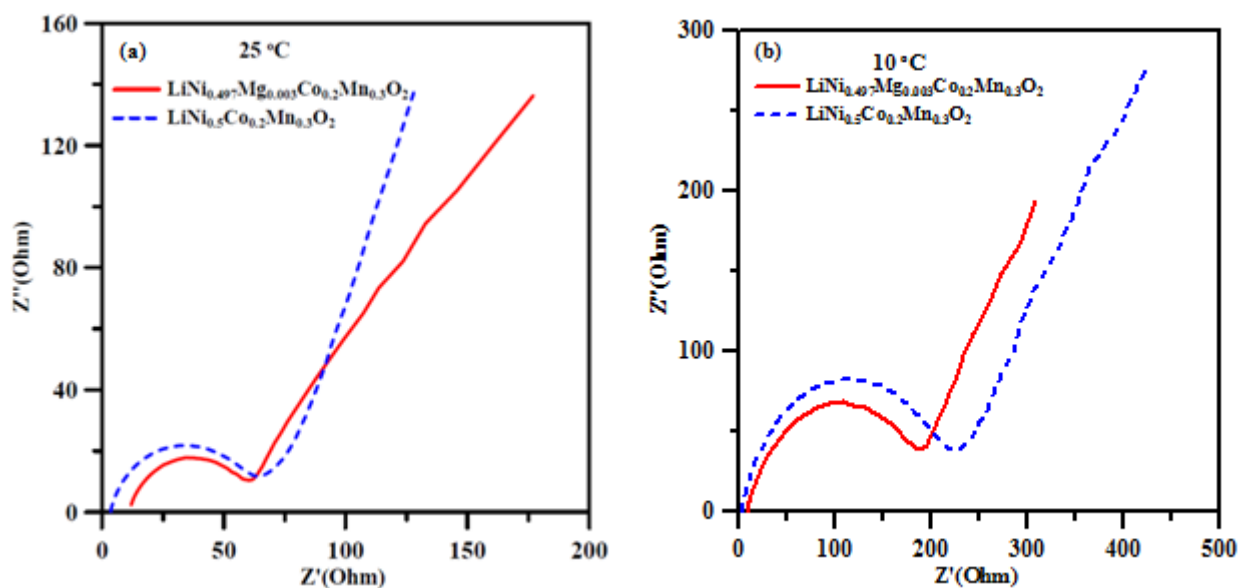


Figure 8. The Nyquist plot of the coin cell using $\text{LiNi}_{0.5}\text{Co}_{0.2}\text{Mn}_{0.3}\text{O}_2$ and $\text{LiNi}_{0.497}\text{Mg}_{0.003}\text{Co}_{0.2}\text{Mn}_{0.3}\text{O}_2$ as the cathode electrode at (a) room temperature and (b) 10°C measurements.

Figs. 8a and 8b show the Nyquist plot of the coin cells after discharged. According to these results, it is clear to indicate that the $\text{LiNi}_{0.497}\text{Mg}_{0.003}\text{Co}_{0.2}\text{Mn}_{0.3}\text{O}_2$ cell provides a smaller semi circle, representing the lower impedance (60.8Ω) of the cell compare to the pristine $\text{LiNi}_{0.5}\text{Co}_{0.2}\text{Mn}_{0.3}\text{O}_2$ (69.1Ω) at room temperature measurement. The same behavior at 10°C measurement, the cell that employed $\text{LiNi}_{0.497}\text{Mg}_{0.003}\text{Co}_{0.2}\text{Mn}_{0.3}\text{O}_2$ electrode shows lower impedance (187.2Ω) compare to the pristine $\text{LiNi}_{0.5}\text{Co}_{0.2}\text{Mn}_{0.3}\text{O}_2$ (228.6Ω) due to the 0.3 mol % of Mg doping in which enhances the ionic diffusion.

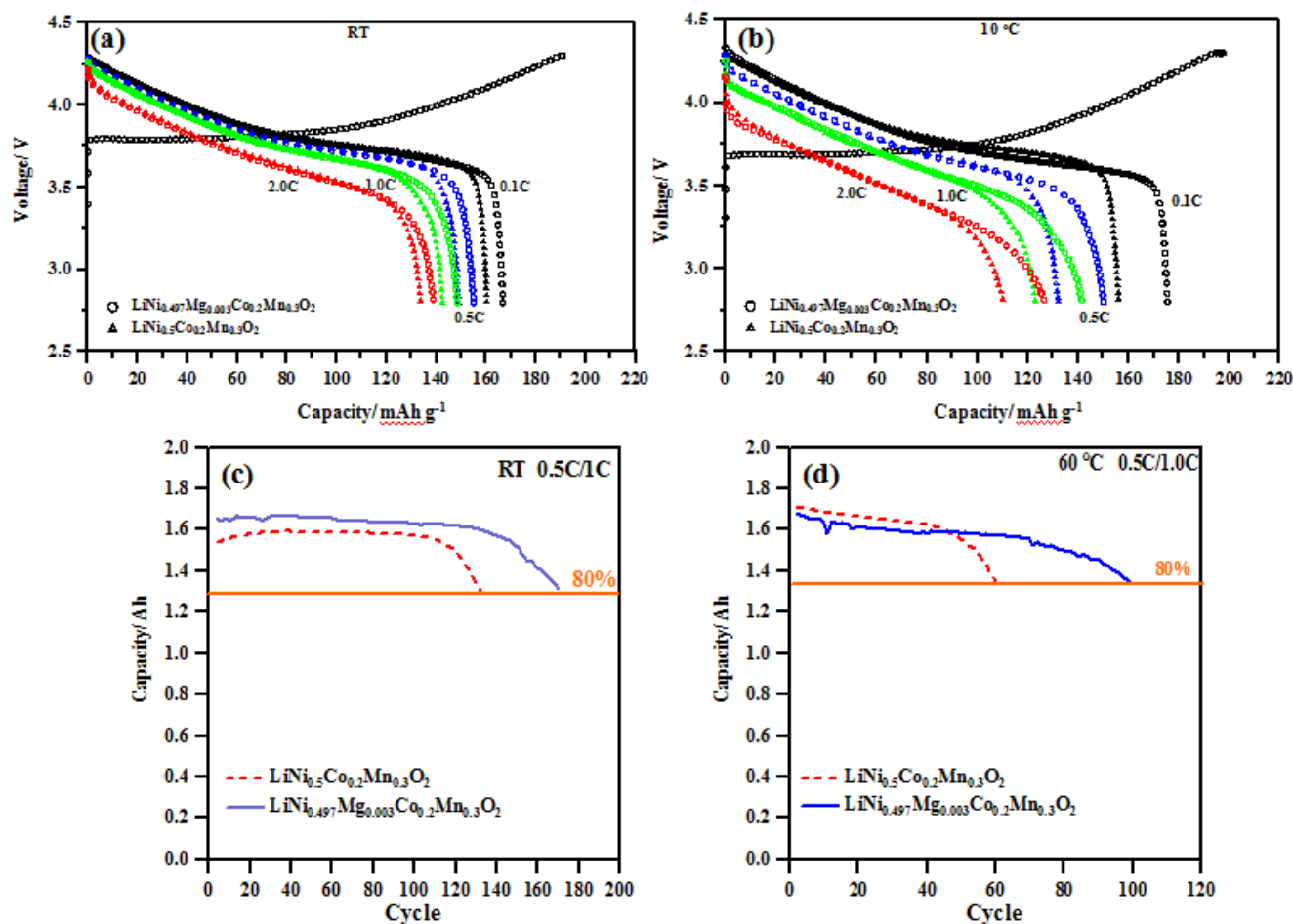


Figure 9. The rate discharge curves of $\text{LiNi}_{0.5}\text{Co}_{0.2}\text{Mn}_{0.3}\text{O}_2$ and $\text{LiNi}_{0.497}\text{Mg}_{0.003}\text{Co}_{0.2}\text{Mn}_{0.3}\text{O}_2$ at (a) room temperature, (b) 10°C and the cycle life test at (c) room temperature, (d) 60°C .

Figs. 9a and 9b show the discharge rate performance of the lithium ion battery at room temperature and at 10°C , respectively. Fig. 9a and Table 1 show that the discharge capacity at 0.1 C of 167 mAh g^{-1} for $\text{LiNi}_{0.497}\text{Mg}_{0.003}\text{Co}_{0.2}\text{Mn}_{0.3}\text{O}_2$ is approximately 4.3% greater than the $\text{LiNi}_{0.5}\text{Co}_{0.2}\text{Mn}_{0.3}\text{O}_2$ of 160 mAh g^{-1} . However, the working voltage plateau of 3.74 V and the open circuit voltage of 4.28 V are the same for both compounds, indicating that the molar ratio of lithium ions in the $\text{LiNi}_{0.497}\text{Mg}_{0.003}\text{Co}_{0.2}\text{Mn}_{0.3}\text{O}_2$ structure is greater than 1. According to the XRD results, the *a*- and *c*-axes of the $\text{LiNi}_{0.497}\text{Mg}_{0.003}\text{Co}_{0.2}\text{Mn}_{0.3}\text{O}_2$ structure are longer than those of $\text{LiNi}_{0.5}\text{Co}_{0.2}\text{Mn}_{0.3}\text{O}_2$, indicating that the unit cell space in the $\text{LiNi}_{0.497}\text{Mg}_{0.003}\text{Co}_{0.2}\text{Mn}_{0.3}\text{O}_2$ structure

can accommodate an excess of lithium ions more effectively than the $\text{LiNi}_{0.5}\text{Co}_{0.2}\text{Mn}_{0.3}\text{O}_2$ interstices can. Thus, the atomic ratio for $\text{LiNi}_{0.5}\text{Co}_{0.2}\text{Mn}_{0.3}\text{Mg}_{0.002}\text{O}_2$ was recalculated based on the improved discharge capacity, and the stoichiometric ratio was redefined to $\text{Li}_{1.1}\text{Ni}_{0.497}\text{Mg}_{0.003}\text{Co}_{0.2}\text{Mn}_{0.3}\text{O}_2$. Fig. 9b and Table 1 show that the improvement in discharge capacity becomes significant at 10 °C. This study attributed these improvements to the increases in ionic diffusion that is a result of Mg doping. The resulting discharge capacity is enhanced by more than 12%. This suggests that doping with Mg generates two benefits that improve capacity: the ability to store more lithium ions, and an increased rate caused by the resulting high electric conductivity of this material.

Table 1. Charge and discharge capacity of (a) $\text{LiNi}_{0.5}\text{Co}_{0.2}\text{Mn}_{0.3}\text{O}_2$ and (b) $\text{LiNi}_{0.497}\text{Mg}_{0.003}\text{Co}_{0.2}\text{Mn}_{0.3}\text{O}_2$ at 0.1C.

Compound	Charge	Discharge	Irr (%)
$\text{LiNi}_{0.5}\text{Co}_{0.2}\text{Mn}_{0.3}\text{O}_2$ ---RT	186	160	26
$\text{LiNi}_{0.497}\text{Mg}_{0.003}\text{Co}_{0.2}\text{Mn}_{0.3}\text{O}_2$ ---RT	191	167	24
$\text{LiNi}_{0.5}\text{Co}_{0.2}\text{Mn}_{0.3}\text{O}_2$ ---10°C	183	156	27
$\text{LiNi}_{0.497}\text{Mg}_{0.003}\text{Co}_{0.2}\text{Mn}_{0.3}\text{O}_2$ ---10°C	195	175	20

Unit: mAh g⁻¹

Table 2. Discharge rate capacity of (a) $\text{LiNi}_{0.5}\text{Co}_{0.2}\text{Mn}_{0.3}\text{O}_2$ and (b) $\text{LiNi}_{0.497}\text{Mg}_{0.003}\text{Co}_{0.2}\text{Mn}_{0.3}\text{O}_2$.

Compound	0.1C	0.5C	1.0C	2.0C
$\text{LiNi}_{0.5}\text{Co}_{0.2}\text{Mn}_{0.3}\text{O}_2$ ---RT	160	149	142	134
$\text{LiNi}_{0.497}\text{Mg}_{0.003}\text{Co}_{0.2}\text{Mn}_{0.3}\text{O}_2$ ---RT	167	155	148	139
$\text{LiNi}_{0.5}\text{Co}_{0.2}\text{Mn}_{0.3}\text{O}_2$ ---10°C	156	132	123	110
$\text{LiNi}_{0.497}\text{Mg}_{0.003}\text{Co}_{0.2}\text{Mn}_{0.3}\text{O}_2$ ---10°C	175	149	141	126

Unit: mAh g⁻¹

Figs. 9c and 9d show the cycle-ability performance at room temperature and at 60 °C, respectively. According to the figures and Table 2, the durability of a cell incorporating $\text{Li}_{1.1}\text{Ni}_{0.497}\text{Mg}_{0.003}\text{Co}_{0.2}\text{Mn}_{0.3}\text{O}_2$ as the cathode material maintains excellent performance. Under 80% retention cycle duration testing, $\text{Li}_{1.1}\text{Ni}_{0.497}\text{Mg}_{0.003}\text{Co}_{0.2}\text{Mn}_{0.3}\text{O}_2$ provided nearly 25% retention at room temperature and 66% retention at 60 °C compared to the retention of $\text{LiNi}_{0.5}\text{Co}_{0.2}\text{Mn}_{0.3}\text{O}_2$ at those temperatures, confirming the DSC and DFT simulation-based forecasts that $\text{Li}_{1.1}\text{Ni}_{0.497}\text{Mg}_{0.003}\text{Co}_{0.2}\text{Mn}_{0.3}\text{O}_2$ is an excellent candidate for electrical vehicle applications.

4. CONCLUSION

$\text{Li}_{1.1}\text{Ni}_{0.497}\text{Mg}_{0.003}\text{Co}_{0.2}\text{Mn}_{0.3}\text{O}_2$ was prepared using a solid-state methodology. Mg doping did not alter the phase from that of the pristine material, and no impurities were observed in the XRD

spectrum. The DSC results of delithiated $\text{Li}_{1.1}\text{Ni}_{0.497}\text{Mg}_{0.003}\text{Co}_{0.2}\text{Mn}_{0.3}\text{O}_2$ indicate superior thermal stability, with a higher temperature exothermic onset reaction compared to that of the pristine material, $\text{LiNi}_{0.5}\text{Co}_{0.2}\text{Mn}_{0.3}\text{O}_2$. Electrochemical testing of 18650 cells revealed that cycle retention is greatly improved over that of the non-doped material, particularly at elevated temperatures. The Mg-modified cells also exhibited excellent discharge rates performance at 10 °C. The current study findings reveal important evidence that Mg doping enhances ionic diffusion and extends the space available within the crystal lattice for excess lithium ions storage. Furthermore, Mg doping minimizes the balance state of energy in the structure, thus improving thermal stability.

ACKNOWLEDGEMENT

This research is supported by the Ministry of Economic Affairs, R.O.C (No.B354DN3100). The authors are also grateful for the financial support from the National Science Council of Taiwan, R. O. C, under Grant NSC 100-2628-E-011-018-MY2, 100-2923-E-011-001-MY3, 102-3113-E-011-002, and 102-ET-E-011-003-ET.

References

1. J. M. Tarascon, M. Armand, *Nature* 414 (2001) 359.
2. B. Scrosati, J. Garche, *J. Power Sources* 195 (2010) 2419.
3. Y. G. Guo, J. S. Hu, L. J. Wan, *Adv. Mater.* 20 (2008) 2878.
4. M. Armand, J. M. Tarascon, *Nature* 451 (2008) 652.
5. P. G. Bruce, *Solid State Ionics* 179 (2008) 752.
6. F. Wu, M. Wang, Y. F. Su, L. Y. Bao, S. Chen, *J. Power Sources* 195 (2010) 2362.
7. T. Ohzuka, R. J. Brodd, *J. Power Sources* 174 (2007) 449.
8. S. W. Oh, S. H. Park, C. W. Park, Y. K. Sun, *Solid State Ionics* 171 (2004) 167.
9. M. Yoshio, H. Noguchi, J. Itoh, M. Okada, T. Mouri, *J. Power Sources* 90 (2000) 176.
10. D. C. Li, Y. Sasaki, M. Kageyama, K. Kobayakawa, Y. Sato, *J. Power Sources* 148 (2005) 85.
11. N. Yabuuchi, T. Ohzuka, *J. Power Sources* 119-121 (2003) 171.
12. Z. Liu, A. Yu, J. Y. Lee, *J. Power Sources* 81-82 (2003) 416.
13. S. H. Park, C. S. Yoon, S. G. Kang, H. S. Kim, S. I. Moon, Y. K. Sun *Electrochim. Acta* 49 (2004) 557.
14. A. Deba, U. Bergmann, S. P. Cramer, E. J. Cairns, *J. Appl. Phys.* 97 (2005) 113523.
15. S. Dou, W. Wang, *J. Solid State Electrochem.* 15 (2011) 399.
16. J. S. Arias, C. V Rao, J. Shojan, A. Manivannan, L. Torres, Y. Ishikawa, R S Katiyar, *J. Power Sources* 211 (2012) 12.
17. P. Y. Liao, J. G. Duh, H. S. Sheu, *J. Power Sources* 183 (2008) 766.
18. B. Lin, Z. Wen, Z. Gu, X. Xu, *J. Power Sources* 174 (2007) 544.
19. K. Yang, L. Z. Fan, J. Guo, X. Qu, *Electrochim. Acta* 63 (2012) 364.
20. D. Vanderbilt, *Phys. Rev. B: Condens. Matter* 41 (1990) 7892.
21. P. E. Blochl, *Phys. Rev. B: Condens. Matter* 50 (1994) 17953.
22. M. C. Payne, M. P. Teter, D. C. Allan, T. A. Arias, J. D. Joannopoulos, *Rev. Mod. Phys.* 64 (1992) 1045.
23. G. Kresse, D. Joubert, *Phys. Rev. B: Condens. Matter* 59 (1999) 1758.
24. P. Hu, D. A. King, S. Crampin, M. H. Lee, M. C. Payne, *Chem. Phys. Lett.* 230 (1994) 501.
25. J. P. Perdew, J. A. Chevary, S. H. Vosko, K. A. Jackson, M. R. Pederson, D. J. Singh, C. Fiolhais, *Phys. Rev. B: Condens. Matter* 46 (1992) 6671.

26. G. Kresse, J. Hafner, *Phys. Rev. B: Condens. Matter* 47 (1993) 558.
27. G. Kresse, J. Furthmuller, *Phys. Rev. B: Condens. Matter* 54 (1996) 11169.
28. G. Kresse, J. Furthmuller, *Comp. Mater. Sci.* 6 (1996) 15..
29. K. Dokko, S. Koizumi, K. Sharaishi, K. Kanamura, *J. Power Sources* 165 (2007) 656.
30. C. W. Lee, Y. K. Sun, J. Prakash. *Electrochim. Acta* 49 (2004) 4425.
31. Y. H. Huang, F. M. Wang, T. T. Huang, J. M. Chen, B. J. Hwang, J. Rick, *Int. J. Electrochem. Sci.*, 7 (2012) 1205.